Available online at www.sciencedirect.com
SCIENCE DIRECT®
Journal of Computational Physics 194 (2004) 215–232
JOURNAL OF COMPUTATIONAL PHYSICS
www.elsevier.com/locate/jcp

Efficient numerical method for the direct numerical simulation of the flow past a single light moving spherical body in transitional regimes

Mathieu Jenny *, Jan Dušek

Institut de Mécanique des Fluides et des solides 2, rue Boussingault, F-67000 Strasbourg, France

Received 13 February 2003; received in revised form 18 September 2003; accepted 22 September 2003

Abstract

An efficient numerical method for solving the coupled system of Navier–Stokes equations and equations of motion of a single spherical particle is presented. It combines a spectral – spectral-element spatial discretization in a cylindrical domain moving translationally with the free particle and particle equations of motion involving hydrodynamic forces integrated on the particle surface. The time discretization is semi-implicit with a third-order accurate explicit treatment of the advective terms and a fully implicit treatment of the remaining linear problem consisting in Stokes-like equations coupled with the particle equations of motion. It is shown that the fully implicit approach is the only way to account for very light spheres. Moreover, no reduction of the time step is necessary. The particle equations of motion are re-formulated as a simple system of six linear equations for six unknowns using the fact that the six components combining the hydrodynamic forces and torques depend linearly on particle translation and angular velocities. They are solved directly and are thus exactly satisfied at each time step. Numerical tests show that the increase of computing costs needed to account for the free sphere degrees of freedom remains within about 20% per time step. The accuracy and resolution independence of the solution are tested at the primary instability threshold and for a strongly supercritical zigzagging trajectory. A partial validation using available experimental results is also presented. Very satisfactory accuracy is shown to be obtained with only a very limited number of azimuthal modes.

AMS: 65M70; 76E09

Keywords: Navier–Stokes equations; Spectral-spectral element methods; Particulate flow; Sedimentation; Fluidization; Instabilities; Transition; Wakes

* Corresponding author. Tel.: +33-390-242-896; fax: +33-388-614-300.
E-mail addresses: jenny@imfs.u-strasbg.fr (M. Jenny), dusek@imfs.u-strasbg.fr (J. Dušek).

0021-9991/$ - see front matter © 2003 Elsevier B.V. All rights reserved.
doi:10.1016/j.jcp.2003.09.004

1. Introduction

In a recent paper [1] we implemented the spectral azimuthal decomposition combined with the spectral element discretization proposed by Tomboulides et al. [2] to significantly reduce the computing costs of a numerical investigation of instabilities in the wake of a fixed sphere. The cost reduction stems from the fact demonstrated in [1] that the spectral azimuthal modes of the decomposition coincide with the non-linear modes of the symmetry breaking instability of the wake. As a consequence for a relatively wide interval of Reynolds numbers (200–500), the series converges so fast that only a very reduced number of modes allow very high accuracy to be reached. The resulting costs of fully 3D simulations are multiplied by a factor of only several units as compared to an axisymmetric (2D) computation. This is particularly important for the investigation of the transition scenario where very long runs are needed to characterize the, often very complex, dynamics.

The knowledge of the transition scenario of a fixed sphere wake is, however, insufficient to provide clues about the behavior of freely ascending or falling particles under the combined action of gravity and buoyancy. The problem attracted recently particular attention in chemical engineering thanks to experiments by Karamanev et al. [3]. It has been shown that especially particles lighter than the surrounding fluid behave very differently from the classical models. The degrees of freedom of the free sphere and those of the wake form a system that also behaves differently from that of a fixed sphere wake [4].

The free spherical particle moving in an asymptotically quiescent fluid represents a simple particulate flow. For this type of flows a wide-spread approach is based on the *arbitrary Lagrange–Euler* (ALE) [5,6] or on the distributed-Lagrange-multiplier (DLM) [7] methodology. For a single particle in an infinite fluid domain the problem can be considerably simplified by working in a moving frame [8] and thus by avoiding moving geometry. The treatment of light particles such as bubbles or very light solid spheres requires, however, a careful approach to time discretization. As pointed out in [4], an explicit treatment even fails to make sense if the particle is infinitely light. As a result, the time splitting approach of the type proposed in [7] is applied to particles heavier than the fluid. A possible method would consist in using an iterative algorithm [5]. However, if transitional regimes are to be investigated, special attention has to be paid to the significant cost increase related to an iterative procedure because of the long runs needed to compute their dynamics. To fully exploit the closeness of the fixed and free particle problem for the investigation of the transition scenario in the system of a single free particle moving in a fluid a special approach is needed.

In this paper we present a numerical method to simulate the trajectory and the wake of a single free spherical particle at computational costs comparable to those of solving the flow past a fixed sphere. The objectives of the method can be summed up as follows:

1. given a semi-implicit Navier–Stokes solver, not to reduce its time step,
2. account for light and infinitely light particles,
3. satisfy exactly the particle motion equations,
4. keep overall computing costs of a time step comparable to those of the time step of the Navier–Stokes solver alone.

2. Non-dimensionalized equations and boundary conditions

A way of describing the flow field past a single moving body consists in computing fluid velocities $\mathbf{v}$ measured with respect to a fixed frame projected onto a moving frame attached to the body [8]. For a spherical particle, the frame need not be rotated to keep a fixed geometry of the computational domain. The latter thus moves translationally with the velocity of the center of mass of the body denoted $\mathbf{u}$. The non-dimensionalization of the gravity–buoyancy flows is based on the characteristic acceleration $g_{\text{eff}} = |\rho_0/\rho - 1|g$ where ρ_0 is the density of the solid particle and ρ that of the fluid, both being considered

homogeneous. g is the norm of the gravitational acceleration vector. Combined with the characteristic length scale given by the particle diameter d the acceleration scale g_{eff} yields the velocity scale $(|\rho_0/\rho - 1|gd)^{1/2}$ which can be used to non-dimensionalize the Navier–Stokes equations in the following way:

$$\frac{\partial \mathbf{v}}{\partial t} + [(\mathbf{v} - \mathbf{u}) \cdot \nabla] \cdot \mathbf{v} = -\nabla \cdot p + \frac{1}{G} \nabla^2 \cdot \mathbf{v} \tag{1}$$

and

$$\nabla \cdot \mathbf{v} = 0. \tag{2}$$

The latter contain a single parameter playing the role of the inverse of the non-dimensionalized viscosity

$$G = \frac{\left[\left|\frac{\rho_0}{\rho} - 1\right| g d^3\right]^{1/2}}{v}, \tag{3}$$

called Galileo number for bubbles [8] or equal to the square root of the Archimedes number introduced in the context of particulate flows (see e.g. [3]). v is the kinematic viscosity of the fluid assumed to be Newtonian. The pressure p is considered without the hydrostatic component. Hydrostatic pressure is accounted for explicitly in the balance of forces acting on the body.

The boundary conditions on the sphere surface S account for the six degrees of freedom of the body, the movement of which is described by the translational velocity of its center of mass ($\mathbf{u}$) and by the instantaneous angular velocity vector ($\mathbf{\Omega}$):

$$\mathbf{v}|_S = \mathbf{u} + \mathbf{\Omega} \times \mathbf{r}|_S, \tag{4}$$

where $\mathbf{r}|_S$ is the position vector of a point of the surface. The computational domain is considered to be cylindrical with the cylinder axis parallel to the vertical direction (see Fig. 1). The axis is oriented opposite to the gravity–buoyancy acceleration so that it points systematically downstream of the body whether the latter is heavier or lighter than the fluid, i.e. the unit vector of the domain axis Oz is $\mathbf{i} = -\text{sgn}(\rho_0/\rho - 1)\mathbf{g}/\|\mathbf{g}\|$. The orientation of the vertical axis of the fixed frame is opposite to that of the

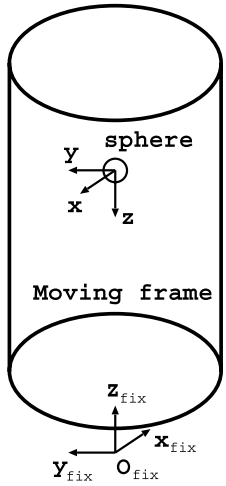

Fig. 1. Geometry of the problem.

moving frame. In the *xyz*-frame moving with the sphere, the fluid enters through the upper cylinder basis in Fig. 1. At this domain boundary the infinite fluid medium is simulated by a uniform velocity condition $\mathbf{v} = 0$. On the lateral surface and on the outflow cylinder basis (the lower one in Fig. 1) a stress–free boundary condition $p = 0, \partial\mathbf{v}/\partial n = 0$ is imposed. This choice of boundary conditions has already been applied with success in the case of a fixed sphere [1].

The Navier–Stokes equations (1) and (2) are coupled to the solid body equations of motion (non-dimensionalized in the same way as (1) and (2)) considered in the fixed frame of Fig. 1:

$$\frac{\rho_0}{\rho}\frac{\mathrm{d}\mathbf{u}}{\mathrm{d}t} = \frac{6}{\pi}\mathbf{F}_{\mathrm{fl}}(\mathbf{v}, p) + \mathbf{k}_{\mathrm{fix}}, \tag{5}$$

$$\frac{\rho_0}{\rho}\frac{\mathrm{d}\mathbf{\Omega}}{\mathrm{d}t} = \frac{60}{\pi}\mathbf{M}_{\mathrm{fl}}, \tag{6}$$

where $\mathbf{k}_{\mathrm{fix}} = -\mathbf{i}$ and $\mathbf{F}_{\mathrm{fl}}$, $\mathbf{M}_{\mathrm{fl}}$ are the hydrodynamic force and torque

$$\mathbf{F}_{\mathrm{fl}} = \int_{\mathrm{S}} \mathbf{f}\,\mathrm{d}S, \tag{7}$$

$$\mathbf{M}_{\mathrm{fl}} = \int_{\mathrm{S}} \mathbf{r}_{\mathrm{S}} \times \mathbf{f}\,\mathrm{d}S, \tag{8}$$

$$f_i = \frac{2}{G}S_{i,j}n_j - pn_i \tag{9}$$

$$S_{i,j} = \left(\frac{\partial v_i}{\partial x_j} + \frac{\partial v_j}{\partial x_i}\right). \tag{10}$$

The coupled system of the Navier–Stokes equations (1) and (2) and of the motion equations (5) and (6) depends on only two dimensionless parameters, the Galileo number G and the reduced density ρ_0/ρ.

3. $U(1)$-representation of transverse cylindrical and cartesian coordinates

The used Navier–Stokes solver is described in [1]. It is formulated in cylindrical coordinates z, r, θ and is based on a spectral–spectral-element discretization using a spectral Fourier decomposition in the azimuthal direction θ and a spectral-element discretization in the r, z-plane. The main problem of the cylindrical coordinates are the geometrical singularities arising at the flow axis. It has been shown [9] that if the usual radial and azimuthal components of velocity, v_r and v_θ, are replaced by complex components $\tilde{v}_\pm = v_r \pm \mathrm{i}v_\theta$ the azimuthal modes have a well defined non-singular behavior at the axis. This allows equations with at worst removable singularities [2] to be obtained. In contrast, the solid body equations of motion will be expressed in Cartesian coordinates with respect to the fixed frame, therefore the velocities $\mathbf{u}$ and $\mathbf{\Omega}$ are systematically given in Cartesian coordinates. This makes it necessary to switch constantly between the modified cylindrical coordinates of [9] and the Cartesian ones. The transformation is, however, easy to describe. Let $\mathbf{A}$ be an arbitrary vector expressed in Cartesian coordinates and in ordinary cylindrical coordinates by (A_z, A_x, A_y) and (A_z, A_r, A_θ), respectively. Introduce $A_\pm = A_x \pm \mathrm{i}A_y$ and $\tilde{A}_\pm = A_r \pm \mathrm{i}A_\theta$. This transformation of the transverse components corresponds to switching from the $O(2)$-representation to the $U(1)$-representation of the rotation group. For brevity we thus refer to $A_\pm$ and $\tilde{A}_\pm$ as to $U(1)$-components. The transformation relation

$$A_r = A_x \cos\theta + A_y \sin\theta,$$

$$A_\theta = -A_x \sin\theta + A_y \cos\theta, \tag{11}$$

then simplifies to

$$\tilde{A}_\pm = A_\pm e^{\mp i\theta}. \tag{12}$$

As a result

$$\tilde{u}_\pm = [u_x \pm i u_y] e^{\mp i\theta}. \tag{13}$$

In what follows, vector and scalar products expressed in $U(1)$-components will be needed. It is easily seen that a vector product can be expressed as

$$\begin{aligned} (\mathbf{A}\times\mathbf{B})_\pm &= \pm i(A_z B_\pm - B_z A_\pm), \\ (\mathbf{A}\times\mathbf{B})_z &= \frac{i}{2}(A_+ B_- - A_- B_+). \end{aligned} \tag{14}$$

The same formula holds both in cylindrical and Cartesian coordinates. Similarly a scalar product can be written as

$$\mathbf{A}\cdot\mathbf{B} = A_z B_z + \frac{1}{2}(A_+ B_- + A_- B_+). \tag{15}$$

4. Fourier azimuthal decomposition

The decomposition of the flow field into a series of Fourier azimuthal modes is defined as follows:

$$p(z,r,\theta,t) = \sum_{m=-\infty}^{+\infty} p_m(z,r,t) e^{-im\theta}, \tag{16}$$

$$\mathbf{v}(z,r,\theta,t) = \sum_{m=-\infty}^{+\infty} \mathbf{v}_m(z,r,t) e^{-im\theta}. \tag{17}$$

It has been shown to be particularly efficient in cases when the tridimensionality originates from axisymmetry breaking being broken. It requires, of course, a computational domain with rotational symmetry. The flow field being real, the pressure and velocity modes satisfy the conditions

$$p_{-m} = \overline{p_m}, \quad v_{z,-m} = \overline{v_{z,m}}, \quad v_{\pm,-m} = \overline{v_{\mp,m}}, \tag{18}$$

showing that only $m \geqslant 0$ modes need to be computed. The velocity field and its azimuthal modes are expressed in $U(1)$-components, so that $\mathbf{v}_m = (v_{z,m}, v_{-,m}, v_{+,m})^T$ (see [1] and, more recently [10]). At the axis, the modes have the following behaviour $(m > 0)$ [2]:

$$v_{z,m}\,|_{r=0} \sim r^m, \quad p_m\,|_{r=0} \sim r^m, \tag{19}$$

$$v_{-,m}\,|_{r=0} \sim r^{m+1}, \tag{20}$$

$$v_{+,m}\,|_{r=0} \sim r^{|m-1|}. \tag{21}$$

Eqs. (1) and (2) are equivalent to the system of equations

$$\frac{\partial v_{z,m}}{\partial t} + \hat{\mathscr{F}}_{m,z} = -\frac{\partial p_m}{\partial z} + \nu \nabla^2_{m^2} v_{z,m}, \tag{22}$$

$$\frac{\partial v_{-,m}}{\partial t} + \hat{\mathscr{F}}_{m,-} = -\left(\frac{\partial p_m}{\partial r} - m\frac{p_m}{r}\right) + \nu \nabla^2_{(m+1)^2} v_{-,m}, \tag{23}$$

$$\frac{\partial v_{+,m}}{\partial t} + \hat{\mathscr{F}}_{m,+} = -\left(\frac{\partial p_m}{\partial r} + m\frac{p_m}{r}\right) + \nu \nabla^2_{(m-1)^2} v_{+,m}, \tag{24}$$

$$\nabla^\dagger_m \cdot \mathbf{v}_m = 0, \tag{25}$$

where $\nabla^\dagger_m$ is minus the divergence operator in the m-subspace

$$-\nabla^\dagger_m = \left(\frac{\partial}{\partial z}, \frac{1}{r}\frac{\partial}{\partial r} r + \frac{m}{r}, \frac{1}{r}\frac{\partial}{\partial r} r - \frac{m}{r}\right), \tag{26}$$

adjoint of the gradient operator ∇_m acting on the pressure mode p_m as written in Eqs. (22)–(24) and where

$$\nabla^2_{m^2} = -\nabla^\dagger_m \cdot \nabla_m. \tag{27}$$

The scalar product $\cdot$ in Eqs. (25) and (27) is to be understood in the sense of Eq. (15). The boundary conditions on the sphere surface (4) involve the spatially constant vectors $\mathbf{u}$ due to the translation of the whole domain. Such a spatially uniform velocity field is converted first to cylindrical coordinates and then transformed to the $U(1)$-representation. The result is equivalent to the complex azimuthal Fourier decomposition will all but $m = 0, 1$ modes. (See Eq. (13) for the transverse components. The axial component remains independent of θ.) If we limit ourselves to $m \geqslant 0$, this yields

$$u_{z,m} = u_z \delta_{m,0}, \tag{28}$$

$$u_{-,m} = 0, \tag{29}$$

$$u_{+,m} = u_+ \delta_{m,1}. \tag{30}$$

Identical relations hold for azimuthal modes of the angular velocity $\mathbf{\Omega}$. By Eq. (12) the cylindrical $U(1)$-components of the position vector $\mathbf{r}$ are (z, r, r). As a result, using the vector product (14)

$$(\mathbf{\Omega} \times \mathbf{r})_{z,m} = \frac{\mathrm{i}}{2} r \Omega_+ \delta_{m,1}, \tag{31}$$

$$(\mathbf{\Omega} \times \mathbf{r})_{-,m} = -\mathrm{i} r \Omega_z \delta_{m,0}, \tag{32}$$

$$(\mathbf{\Omega} \times \mathbf{r})_{+,m} = \mathrm{i}(r\Omega_z \delta_{m,0} - z\Omega_+ \delta_{m,1}). \tag{33}$$

The non-linear terms $\hat{\mathscr{F}}_m$ couple Eqs. (22)–(24) for different azimuthal wave-numbers m. They are written explicitly in the Appendix of the paper [1] for the advective term $(\mathbf{v} \cdot \nabla)\mathbf{v}$. The only modification consists in replacing this term by $[(\mathbf{v} - \mathbf{u}) \cdot \nabla]\mathbf{v}$. This modification is implemented in a straightforward way by sub-

tracting the spatial constants (28), (30) from the corresponding components of the $m = 0$ and $m = 1$ modes of the first factor in the advective terms.

5. Force and torque

The force and torque (7), (8) depend linearly on the flow field therefore their mth azimuthal mode involves only the mth mode of the flow-field. The $U(1)$-components of the mth mode of the deformation velocity tensor are

$$S_{zz,m} = \frac{\partial v_{z,m}}{\partial z}, \tag{34}$$

$$S_{z\pm,m} = \frac{1}{2}\left[\left(\frac{\partial}{\partial r} \pm \frac{m}{r}\right)v_{z,m} + \frac{\partial v_{\pm,m}}{\partial z}\right], \tag{35}$$

$$S_{--,m} = \left(\frac{\partial}{\partial r} - \frac{m+1}{r}\right)v_{-,m}, \tag{36}$$

$$S_{-+,m} = \frac{1}{2}\left[\left(\frac{\partial}{\partial r} + \frac{m+1}{r}\right)v_{-,m} + \left(\frac{\partial}{\partial r} - \frac{m-1}{r}\right)v_{+,m}\right], \tag{37}$$

$$S_{++,m} = \left(\frac{\partial}{\partial r} + \frac{m-1}{r}\right)v_{+,m}. \tag{38}$$

By Eqs. (19)–(21) there are, at worst, removable singularities at the axis $r = 0$.

The cylindrical $U(1)$-components of the force per unit surface are then

$$\tilde{f}_{z,m} = (2\mu S_{zz,m} - p)n_z + \mu(S_{z-,m} + S_{z+,m})n_r, \tag{39}$$

$$\tilde{f}_{-,m} = 2\mu S_{z-,m}n_z + [\mu(S_{-+,m} + S_{--,m}) - p]n_r, \tag{40}$$

$$\tilde{f}_{+,m} = 2\mu S_{z+,m}n_z + [\mu(S_{-+,m} + S_{++,m}) - p]n_r, \tag{41}$$

where n_z and n_r are the axial and radial coordinates of the normal to the surface. Expressions (39)–(41) result from the contraction of the deformation velocity tensor (34)–(38) by the components of the normal vector n_z and $n_\pm$. The surface being axisymmetric, $n_\theta = 0$ and $n_\pm = n_r$.

The torque per unit surface is now given by

$$\tilde{m}_{z,m} = \frac{\mathrm{i}r}{2}\left(\tilde{f}_{-,m} - \tilde{f}_{+,m}\right), \tag{42}$$

$$\tilde{m}_{-,m} = \mathrm{i}\left(r\tilde{f}_{z,m} - z\tilde{f}_{-,m}\right), \tag{43}$$

$$\tilde{m}_{+,m} = \mathrm{i}\left(z\tilde{f}_{+,m} - r\tilde{f}_{z,m}\right). \tag{44}$$

The solid body motion equations being expressed in Cartesian coordinates these quantities have to be transformed via Eq. (12). This brings about a factor $\mathrm{e}^{\pm\mathrm{i}\theta}$ for the Cartesian $\pm$ components. After integration

over θ, only the mode $m = 0$ yields a non-zero contribution to the axial component and the mode $m = 1$ to the $\pm$ components of the total force and torque integrated over the whole sphere surface

$$F_z = 2\pi \int f_{z,0}\,\mathrm{d}s, \tag{45}$$

$$F_- = 2\pi \int \bar{\tilde{f}}_{+,1}\,\mathrm{d}s, \tag{46}$$

$$F_+ = 2\pi \int \tilde{f}_{+,1}\,\mathrm{d}s, \tag{47}$$

$$M_z = 2\pi \int m_{z,0}\,\mathrm{d}s, \tag{48}$$

$$M_- = 2\pi \int \bar{\tilde{m}}_{+,1}\,\mathrm{d}s, \tag{49}$$

$$M_+ = 2\pi \int \tilde{m}_{+,1}\,\mathrm{d}s. \tag{50}$$

The integrals obtained are one-dimensional curvilinear quadratures along spectral element boundaries in the z, r-plane evaluated by the associated Gauss–Lobatto integration.

6. Time discretization

The time discretization is based on the time splitting scheme for the Navier–Stokes equations (22)–(24) presented in [1]. At the first step, the advective terms are treated explicitly using the third order Adams–Bashforth discretization. This yields a linear Stokes-like problem coupled to the equations of motion which can be expressed schematically as

$$\mathbf{I}\frac{\mathrm{d}\mathbf{Y}}{\mathrm{d}t} = \mathbf{M}\mathbf{Y} + \mathbf{G}, \tag{51}$$

where

$$\mathbf{Y} \equiv \begin{bmatrix} \mathbf{U} \\ \mathbf{P} \\ \mathbf{Z} \end{bmatrix}, \quad \mathbf{M} \equiv \begin{bmatrix} \mathbf{L} & \mathbf{D} & \mathbf{H} \\ \mathbf{D}^\dagger & 0 & 0 \\ \mathbf{B} & \mathbf{C} & 0 \end{bmatrix}, \quad \mathbf{G} \equiv \begin{bmatrix} \mathbf{N} \\ 0 \\ \mathbf{K} \end{bmatrix}, \tag{52}$$

and $\mathbf{I}$ is equal block-wise to $\mathrm{diag}(\mathbf{1}, \mathbf{0}, \rho_0/\rho\mathbf{1})$. $\mathbf{U}$ and $\mathbf{P}$ stand, respectively, for the discretized velocity and pressure field and $\mathbf{Z} \equiv (\mathbf{u}, \mathbf{\Omega})^{\mathrm{T}}$ is the six-dimensional array of sphere velocities. $\mathbf{L}$ discretizes the diffusion terms, $\mathbf{D}$ the pressure gradient, $\mathbf{H}$ the boundary conditions on the sphere surface, $\mathbf{B}$ and $\mathbf{C}$ the viscous and pressure terms of the hydrodynamic force and torque. The inhomogeneous term includes the buoyancy force $\mathbf{K} = (\mathbf{k}, 0)^{\mathrm{T}}$ and the explicitly treated non-linear terms $\mathbf{N}$. This is a standard matrix problem associated to particulate flow equations (see [5,7]). While, for the reasons of numerical stability, an implicit treatment is usually desirable, this objective is either paid for by an expensive iterative procedure (as in [5], the iterative procedure allowing the non-linear terms to be included into the iterations in this case) or is

subject to some compromise. For example, in [7] the treatment of repulsive forces requires most attention and reduces considerably the time step. As a consequence, for particles heavier than the fluid, an explicit treatment of hydrodynamic forces is found satisfactory.

In our case, however, if very light particles are to be accounted for without restriction of the time step, it is obvious that an explicit treatment of Eqs. (5) and (6) will not work. For infinitely light particles the equations of motion of the solid body (5), (6) or, equivalently, the last six equations of the system (51), play the same role of constraint as the continuity equation. In that case, the implicit treatment is the only treatment possible. As for the diffusion terms, the fully implicit treatment seems to be rather commonly used in particulate flows (see e.g. [7]). For relatively low viscosities, i.e., in the present case, high Galileo numbers (in the hundreds) and for a fine discretization of the boundary layer at the sphere surface (the nearest collocation point lies $0.01d$ from the sphere surface) implying a rather short time step a first order fully implicit treatment of the diffusion terms provides good accuracy (see [1]) and guarantees good numerical stability. To treat problem (51) in the fully implicit way

$$\mathbf{I}\frac{\mathbf{Y}^{(n+1)}-\mathbf{Y}^{(n)}}{\Delta t}=\mathbf{M}\mathbf{Y}^{(n+1)}+\mathbf{G}, \tag{53}$$

we first remark that the coupling between the flow-field and the motion equations is effective only for the $m=0$ and $m=1$ modes. To obtain the sphere velocities, system (53) needs to be solved merely with account of these two modes. The solution is split into two terms

$$\mathbf{v}^{(n+1)}=\mathbf{v}_0^{(n+1)}+\Delta\mathbf{v}^{(n+1)}, \tag{54}$$

$$p^{(n+1)}=p_0^{(n+1)}+\Delta p^{(n+1)}, \tag{55}$$

where $\mathbf{v}_0^{(n+1)}$ (resp. $p_0^{(n+1)}$) is the solution of the problem with the boundary conditions involving the solid body velocities obtained at the nth step and $\Delta\mathbf{v}^{(n+1)}$ (resp. $\Delta p^{(n+1)}$) is the correction accounting for the variation of the boundary conditions. If we denote $\mathbf{U}_0^{(n+1)},\mathbf{P}_0^{(n+1)}$ and $\Delta\mathbf{U}^{(n+1)},\Delta\mathbf{P}^{(n+1)}$ the discretized counterparts of the fields represented, respectively, by the first and second terms on the RHS of Eqs. (54) and (55), the intermediate discretized solution satisfies (see Eq. (52) for details of notation)

$$\frac{1}{\Delta t}\begin{bmatrix}\mathbf{U}_0^{(n+1)}-\mathbf{U}^n\\ 0\end{bmatrix}=\begin{bmatrix}\mathbf{L} & \mathbf{D}\\ \mathbf{D}^\dagger & 0\end{bmatrix}\begin{bmatrix}\mathbf{U}_0^{(n+1)}\\ \mathbf{P}_0^{(n+1)}\end{bmatrix}+\begin{bmatrix}\mathbf{H}\mathbf{Z}^{(n)}+\mathbf{N}\\ 0\end{bmatrix}, \tag{56}$$

where $\mathbf{U}^n$ and $\mathbf{Z}^{(n)}$ are the known discretized flow field and sphere velocities obtained at the previous time step. The corrections are the solution of a linear system coupling the flow field corrections $\Delta\mathbf{U}^{(n+1)}$, $\Delta\mathbf{P}^{(n+1)}$ and the velocity correction

$$\mathbf{X}=\begin{pmatrix}\mathbf{u}^{(n+1)}-\mathbf{u}^{(n)}\\ \boldsymbol{\Omega}^{(n+1)}-\boldsymbol{\Omega}^{(n)}\end{pmatrix}. \tag{57}$$

This system reads

$$\frac{1}{\Delta t}\begin{bmatrix}\Delta\mathbf{U}^{(n+1)}\\ 0\end{bmatrix}=\begin{bmatrix}\mathbf{L} & \mathbf{D}\\ \mathbf{D}^\dagger & 0\end{bmatrix}\begin{bmatrix}\Delta\mathbf{U}^{(n+1)}\\ \Delta\mathbf{P}^{(n+1)}\end{bmatrix}+\begin{bmatrix}\mathbf{H}\mathbf{X}\\ 0\end{bmatrix}, \tag{58}$$

$$\frac{\rho_0}{\rho}\frac{1}{\Delta t}\mathbf{X}=\mathbf{B}\Delta\mathbf{U}^{(n+1)}+\mathbf{C}\Delta\mathbf{P}^{(n+1)}+\mathbf{R}, \tag{59}$$

where $\mathbf{R}$ is the residual of the motion equations in which the forces are calculated using the intermediate flow-field

$$\mathbf{R} = \begin{pmatrix} \frac{6}{\pi}\mathbf{F}_{\mathrm{fl}}(\mathbf{v}_0^{(n+1)}, p_0^{(n+1)}) + \mathbf{k}_{\mathrm{fix}} \\ \frac{60}{\pi}\mathbf{M}_{\mathrm{fl}}(\mathbf{v}_0^{(n+1)}, p_0^{(n+1)}) \end{pmatrix}. \tag{60}$$

Eq. (56) is the Stokes-like problem as it would anyway be solved by the Navier–Stokes solver. The purpose being the computation of residual (60), i.e. the computation of the hydrodynamic force and torque, for which only azimuthal modes $m = 0, 1$ are needed, the Stokes-like problem (56) can be restricted to azimuthal modes $m = 0, 1$.

Eq. (58) is the discretized counterpart of the Stokes-like problem

$$\frac{\Delta\mathbf{v}^{(n+1)}}{\Delta t} + \nabla \cdot \Delta p^{(n+1)} + \frac{1}{G}\nabla^2 \cdot \Delta\mathbf{v}^{(n+1)} = 0, \tag{61}$$

$$\nabla \cdot \Delta\mathbf{v}^{(n+1)} = 0, \tag{62}$$

with the boundary conditions

$$\Delta\mathbf{v}|_{\mathrm{S}} = \begin{bmatrix} 1 & 0 & 0 & 0 & y|_{\mathrm{S}} & -x|_{\mathrm{S}} \\ 0 & 1 & 0 & -y|_{\mathrm{S}} & 0 & z|_{\mathrm{S}} \\ 0 & 0 & 1 & x|_{\mathrm{S}} & -z|_{\mathrm{S}} & 0 \end{bmatrix} \mathbf{X}, \tag{63}$$

where $(z|_{\mathrm{S}}, x|_{\mathrm{S}}, y|_{\mathrm{S}})$ is the position of a given point on the sphere surface. Writing formally the solution of Eq. (58) as a function of the the velocity updates $\mathbf{X}$ in the form $\Delta\mathbf{U}^{(n+1)} = \mathbf{S}\mathbf{X}$, $\Delta\mathbf{P}^{(n+1)} = \mathbf{T}\mathbf{X}$ and denoting $\mathbf{A}$ the 6×6 matrix $\mathbf{BS} + \mathbf{CT}$ we arrive at a simple linear relation between residual (60) and the velocity correction

$$\left(\frac{\rho_0}{\rho}\frac{1}{\Delta t} - \mathbf{A}\right)\mathbf{X} = \mathbf{R}. \tag{64}$$

The six columns of the matrix $\mathbf{A}$ are computed as the forces and torques in response to unit variations of translation velocities in each spatial direction and of angular velocities around the three axes. These variations yield the six different boundary conditions described by the columns of the matrix on the RHS of Eq. (63). Again, for the computation of forces only the modes $m = 0, 1$ are needed. In other words, we solve the Stokes-like problem (61)–(63) (restricted to $m = 0, 1$) for these six distinct boundary conditions. The matrix $\mathbf{A}$ does not vary if Δt is not modified. It has to be recalculated only if the time step changes to meet the CFL criterion. This occurs very rarely, typically only at beginning of the acceleration if a trajectory starting at rest is computed. A run of tens thousands of time steps may involve just one computation of the matrix $\mathbf{A}$.

The new sphere velocities being known, problem (61)–(63) is finally solved for all desired azimuthal modes. If the azimuthal discretization is truncated at, say, $m_{\max} = 6$ the preliminary computation of the residual (60) involving only modes $m = 0, 1$ represents only a fraction of the overall cost of a time step.

7. Numerical tests

In the absence of available bibliographical references (the only numerical paper dealing with a closely related subject is [8]) the validation of the algorithm is based on:

(i) reference to the well-known results concerning the fixed sphere wake (validated themselves in [1]),
(ii) proofs of numerical convergence of sample simulation results and on
(iii) an experimental validation in a laboratory water tank [11].

In the same way as in [1] the physics of the problem makes it logical to proceed in the order of increasing complexity of the simulated regimes.

7.1. Primary bifurcation

The primary bifurcation of the system represented by the sphere wake coupled with the degrees of freedom of the sphere has been investigated in a recent paper [4]. The method of linear analysis of the axisymmetric flow is described in [1]. The implementation of the spectral azimuthal expansion allows for an arbitrary truncation. In particular it is possible to reduce the expansion to a single azimuthal mode $m \neq 0$. This removes the coupling between the investigated mode and the axisymmetric one ($m = 0$) filled with the precalculated base flow and allows to investigate the most unstable eigenvalue separately in each m-subspace into which the eigenvalue problem has been shown to break up. As can be seen from Eqs. (30), (31), (33), (46), (47), (49), (50), for a free sphere, the transverse velocity components are coupled to the $m = 1$ mode. As shown in [4] the $m = 1$ azimuthal mode remains the most unstable: the lighter the sphere the more the degrees of freedom of the sphere enhance the instability. The value of the most unstable eigenvalue or, equivalently, the threshold of the primary bifurcation provides a good test of the quality of the spectral element mesh in the r–z-plane. It is not surprising that the same mesh as that used in [1] for analyzing the instability of the fixed sphere wake yields a good accuracy. For very dense spheres $\rho_0/\rho \to \infty$, for which the degrees of freedom of the sphere play no role a critical Galileo number $G_{\mathrm{crit}} = 159.3$ equivalent to the asymptotic Reynolds number of 211.9, very close the widely adopted value [12], is obtained. For light spheres, for which no reference for comparison exists yet, the values published in [4] ($G_{\mathrm{crit}} = 156.1$ for $\rho_0/\rho = 0.5$ and $G_{\mathrm{crit}} = 155.8$ for $\rho_0/\rho = 0$) have been tested for insensitivity to further mesh refinement and domain extension. The explanation why the mesh used for the fixed sphere wake is so satisfactory comes from the fact that the unstable modes of the fixed sphere and the fluid part of the free sphere mode (the unstable mode represented in terms of the fluid velocity and pressure field) are very similar (see Fig. 2) and the refined subdomain of the "reference" mesh represented in Fig. 6(a) covers well the extent of the mode whatever the reduced density.

In [4] it has been shown that the primary bifurcation leads to a non-axisymmetric steady state characterized by an asymptotically straight and oblique trajectory. An experiment we set up together with Bouchet [11] in our laboratory has been designed to study the trajectories of freely ascending or falling

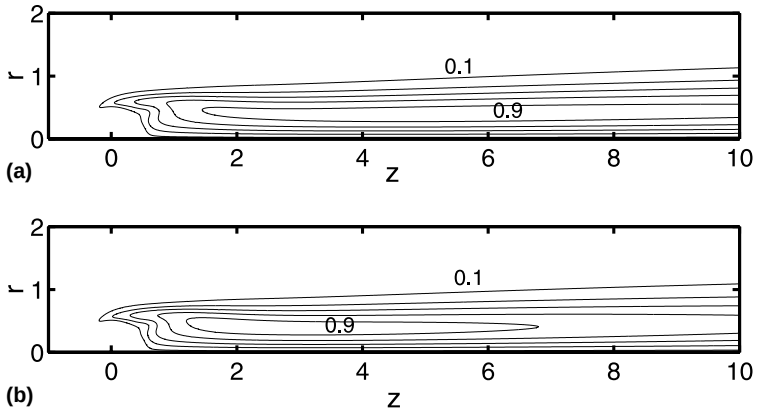

Fig. 2. Iso-values of axial velocity the most unstable linear mode mode ($m = 1$) computed at the threshold of the primary instability (respectively at $G = 156$ and $G = 160$) for $\rho_0/\rho = 0$ (a) and $\rho_0/\rho = \infty$ (b). The modes are normalized so that the maximum is equal to 1.

spheres experimentally. The fine tuning of the experiment being somewhat tricky, at this moment we have only several more or less random samples of different regimes in the parameter space $(\rho_0/\rho, G)$ at our disposal. Fortunately, there is an easily exploitable sample of trajectories corresponding precisely to this steady oblique regime. The experimental sphere (a polypropylene bearing ball of 3.16 mm of diameter and of density $\rho_0 = 890$ kg/m^3, $\rho_0/\rho = 0.89$) is released at the bottom of a water tank of section 0.5 m times 0.5 and 2.5 m of height (see [11] for more details). The viscosity of water is driven by its temperature. At 17.6 °C we reached a Galileo number of 173. The trajectory is obtained by processing of images of two cameras tracking the particle. The processing of two images allows the trajectories to be fully determined in 3D. For exactly these same values of problem parameters we computed a trajectory starting at rest and reaching the asymptotic steady regime. Both the experimental and the numerical results are plotted in Fig. 3. The trajectories are represented in Fig. 3(a). The onset of instability is better visible on the plot of the horizontal velocity versus time (Fig. 3(b)). The experimental trajectory does not start exactly at rest. The sphere is initially held to the extremity of a capillary tube by depression. At the moment when it is released by an increase of pressure in the tube, a slight push of a simultaneously escaping small air bubble cannot be avoided. Moreover, the particle tracking does not start exactly at the point of release. The agreement is very satisfactory. Both the simulation and the image processing capture also the oscillatory transients due to the proximity of the secondary Hopf bifurcation. The vertical asymptotic velocity of the sphere is 1.34 in the units defined in Section 2. Note that the Strouhal number of these oscillations ($St = fd/U_\infty$) is 0.040, i.e. significantly smaller than for the wake of a fixed sphere. This trend is in a rather good agreement with the experimental result of [13] concerning spherical bubbles with a not perfectly clean interphase. It is widely accepted that such bubbles can be assimilated to infinitely light solid spheres.

7.2. Strongly supercritical trajectories

In terms of trajectories, the primary bifurcation yields an oblique straight-line ascension of light spheres. The simulations and the preliminary experiments [4,11] show that a secondary Hopf bifurcation follows the regular primary one. It generates a wavy oblique trajectory which ends up by switching to a zigzagging vertical motion as soon as the amplitude of the secondary oscillations of the horizontal velocity compensates the mean value. This rather strongly supercritical regime (see Figs. 4 and 5) at which new interesting physics can be investigated has been taken as a basis for further numerical tests. The influence of

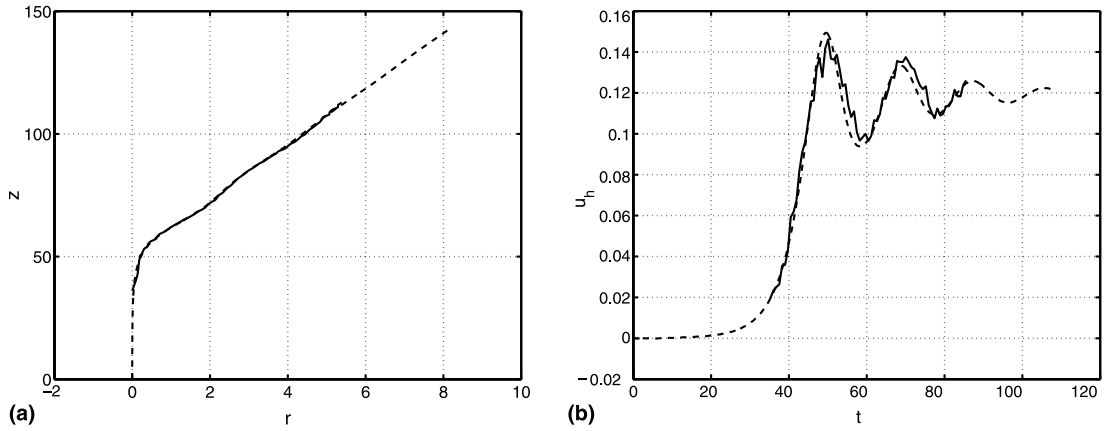

Fig. 3. Experimental (solid line) and numerical trajectory (dashed line) for a density ratio $\rho_0/\rho = 0.89$ and $G = 173$. (a) The trajectory, (b) the horizontal projection of the velocity vs. time (in units defined in Section 2).

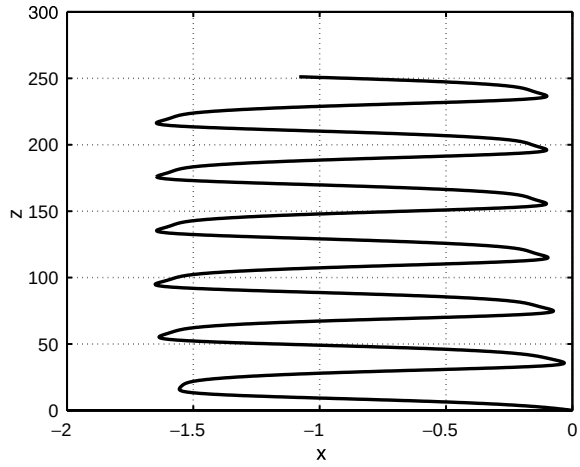

Fig. 4. "Zigzagging" trajectory obtained using the "final" mesh of Fig. 6, for $G = 200$ and $\rho_0/\rho = 0.5$ ($m_{\max} = 6$).

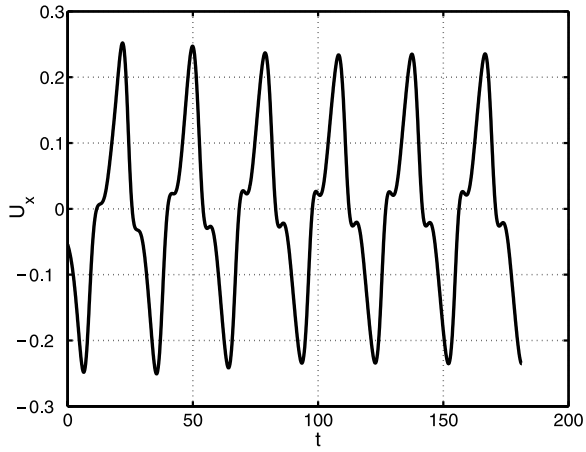

Fig. 5. Horizontal velocity of the trajectory described in Fig. 4.

various parameters of the discretization on the results of the simulation at $G = 200$ and for the density ratio $\rho_0/\rho = 0.5$ has been studied.

7.2.1. Additional spectral element mesh testing

The z–r-plane mesh of [1] used for the investigation of the primary bifurcation is chosen as the "reference mesh" (see Fig. 6). Note that only the spectral-elements are represented, not the internal collocation points. In our simulation, each spectral element contains 6×6 collocations points. The dependence on the number of collocation points was tested in [1]). The stronger non-linearities might result in a very oblique wake for which the lateral boundary might influence the simulation results. In the absence of experimental or other numerical data relevant for this regime, we submitted the numerical results to additional tests of numerical convergence. The main issue being the capture of the increasingly oblique wake we focus on two parameters: the role of the lateral numerical boundaries and the number of azimuthal modes needed to reach convergence.

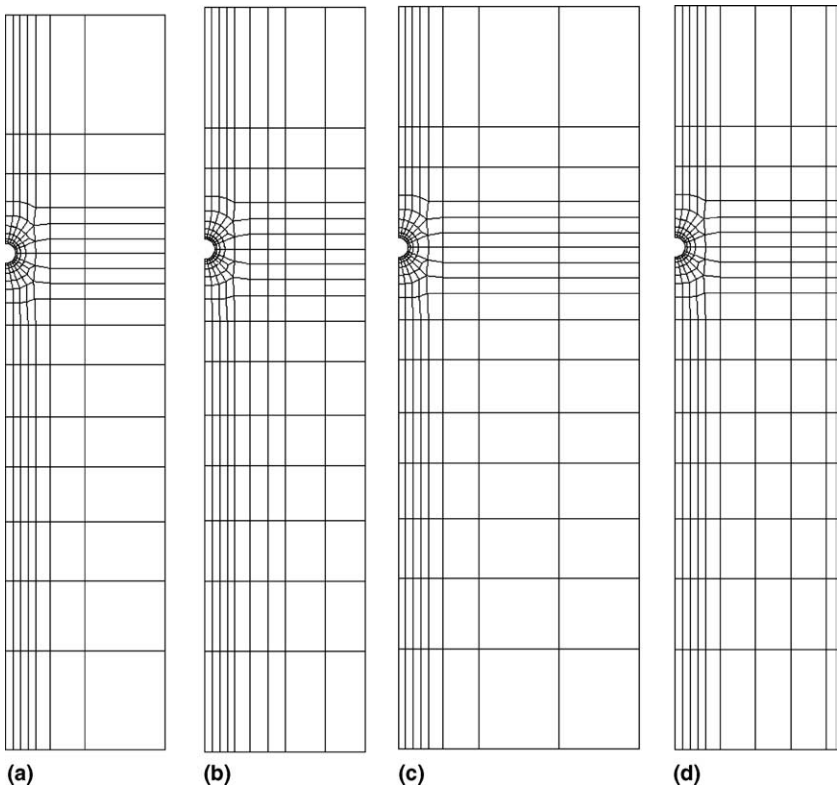

Fig. 6. Breakup into spectral elements tested. In all cases the mesh extends 12 sphere diameters upstream and 25 diameters downstream of the sphere center. (a) Reference mesh (radius 8d), (b) refined mesh (radius 8d), (c) large mesh (radius 12d) and (d) final mesh (radius 8d).

As for the lateral "confinement", we test a "large" mesh (186 elements) with a radius of 12 diameters (compared to 8 diameters) (Fig. 6). Similarly, steeper gradients might not be sufficiently resolved if they fall onto the coarse part of the mesh. A "fine" mesh (Fig. 6) defined within the reference domain with additional elements placed along the lateral limits of the wake (203 elements compared to 169) is also tested. The results are presented in Table 1.

If the meshes were far from optimal the adjustments tested above would bring up non-negligible changes in the results. This is not the case. Table 1 shows that increasing the domain or refining the mesh does not influence the results. The reference mesh allows to obtain a good accuracy but a stability problem occurs during some calculations. The polynomial interpolation in large elements at outer boundary combined with

Table 1
Amplitude and period of the sphere horizontal velocity for different spectral element meshes, for six collocation points in each spatial direction and $m_{\max} = 3$ in the zigzagging regime at $G = 200$ and for $\rho_0/\rho = 0.5$

Mesh	Amplitude	Period, T
Reference	0.2396	30.8677
Fine	0.2396	30.8711
Large	0.2396	30.8818
Final	0.2394	30.9120

the no-stress boundary condition appear to generate numerical instabilities in strongly supercritical regimes. The problem has been resolved by adding a finer layer of spectral elements along the outer boundary as shown in Fig. 6(d).

The characteristics presented in Table 1 are not substantially modified if 8×8 instead of 6×6 collocation points per element are used while the computing costs increase roughly by a factor of three. Indeed, already in paper [1] it appeared to be better to keep the number of collocation points low and distribute the computational effort optimally throughout the domain by putting small elements in regions where velocity gradients are significant.

7.2.2. Convergence of the azimuthal Fourier series

The trajectory and horizontal velocity represented in Figs. 4 and 5 have been obtained on the "final" mesh with the azimuthal decomposition truncated at $m_{\max} = 6$. For an increasing number of azimuthal modes the following parameters are tested: the amplitude of the horizontal velocity, the period and the amplitude of the secondary peak appearing every time the trajectory crosses the mean vertical direction. The azimuthal Fourier modes coincide with the non-linear modes of the primary instability. It has thus to be expected that at higher supercritical regimes the convergence of the series will be slower. The results are presented in Table 2.

As expected, unlike for a fixed sphere wake, for which four azimuthal modes allowed to obtain the secondary instability amplitude with an extremely good precision (better than 1%), more azimuthal modes are needed to simulate the regime represented in Figs. 4 and 5 with a comparable accuracy. The convergence of the series remains, however, very good.

7.3. Chaotic regime

Experiments [14] and [11] indicate that a chaotic behavior is ultimately reached when G increases. There is, so far, no existing reference for validating the chaotic trajectories quantitatively but the algorithm is manifestly able to reproduce such a behavior. In Fig. 7 a trajectory of light sphere ($\rho_0/\rho = 0.5$) in a chaotic regime at $G = 220$ is plotted. Note the intermittent nature of the trajectory also remarked in [14].

7.4. Computational costs

The simulation of the fixed sphere, discussed in [1], is used as a reference case in terms of computational cost. The main difference between the fixed and free sphere cases, in terms of algorithm, consists in solving twice the Stokes-like problem for the modes 0 and 1 in the free sphere case. With, say, seven azimuthal modes (0–6) accounted for, the CPU time needed for one time step decreases by only 15.0% if the computation of the sphere velocities is switched off. This can be considered as a measure of the real computing

Table 2
Evolution of the characteristics of the sphere horizontal velocity with increasing number of azimuthal modes, $G = 200$, $\rho_0/\rho = 0.5$, "reference" mesh of Fig. 6

Azimuthal mode number	Amplitude	Period, T
3	0.2396	30.8677
4	0.2419	29.2800
5	0.2397	29.0029
6	0.2345	29.1818
8	0.2311	29.3489
10	0.2299	29.4560

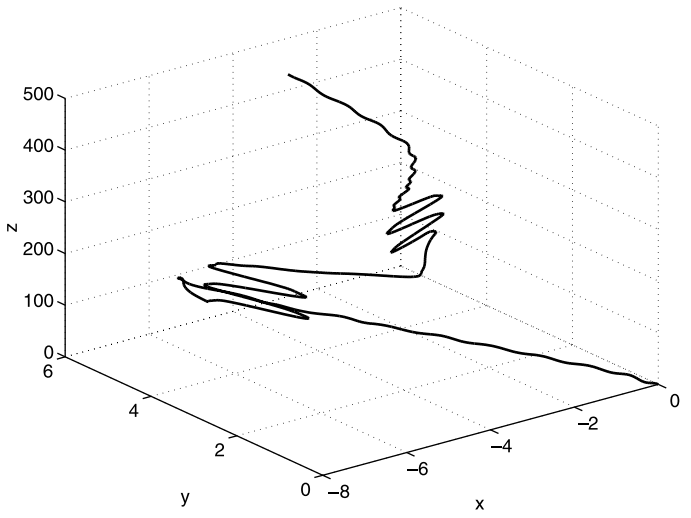

Fig. 7. Chaotic and tridimensional trajectory at $G = 220$ and $\rho_0/\rho = 0.5$.

cost increase because the time step is the same whether the sphere is fixed or free. Of course, due to the variable number of internal iterations of the conjugate gradient solver of the pressure and velocity equations, this value is only indicative. A more realistic comparison consists in solving the fixed- and the free-sphere problems at the same mean Reynolds number. For heavy spheres the hydrodynamic behavior is not very different and the comparison gives a reasonable idea of the cost of the computation of the degrees of freedom of the particle. At $G = 200$ (mean asymptotic $Re = 280$) and for $\rho_0/\rho = 10$ the CPU costs are 20% higher for the free sphere. The necessity to keep the increase of computing costs within limits is clearly illustrated if the physical time scales are considered. At $G = 200$ one period of the wake and trajectory oscillation of a light sphere $\rho_0/\rho < 1$ (see Figs. 4 and 5) is about 5.25 times longer than the period of a heavy sphere $\rho_0/\rho = 10$ or a fixed sphere. The simulation of one period in Figs. 4 and 5 on a Pentium4 1.8 GHz processor lasts $19h$. For the simulation represented in Fig. 7 representing a physical time equivalent to 58 periods of a fixed sphere wake, 162 CPU hours were necessary. Given the low cost of PC processors such a study is easily feasible. A meta-computing network appeared to be particularly suitable for the purpose. The investigation has to be carried out in a two-dimensional parameter space and the physics of the transition appears to be rather complex so that its presentation does not fit into the scope of this paper.

8. Conclusion

In this paper we tackled the problem of the simulation of a single freely moving particle in transitional regimes. In particular light particles present a physically interesting behavior while being potentially difficult to account for. The necessity to ensure good space-time resolution and to provide reliable data on the varying and complex dynamics characterizing the transition adds special requirements on the numerical efficiency of the numerical method. We showed that, in transitional regimes, the efficiency of the simulation of light particles depends on the possibility of a fully implicit treatment of the particle equations of motion. This treatment is implemented using a predictor-corrector approach based on the direct solution of the particle velocities. Numerical tests applied to the simulation of the trajectory of a spherical particle show that the increase of costs due to accounting for the coupling between the flow field and the particle motion represents only about 20%, and even infinitely light particles are accounted for at the same costs.

The implicit approach to the particle equations of motion can be transposed in a straightforward manner to other particle configurations with general 3D geometries. The paper describes how to treat the coupling between the flow equations and the equations of motion of a particle and draws attention to the problem of numerical stability of the equations of motion for light particles. The problem is of general character and the proposed solution is independent of the underlying Navier–Stokes solver. The presentation is based, of course, on a concrete implementation for one particular NS solver, however, mainly the general, NS solver independent, features are focused upon. The described implementation aims at investigating a very special physics: that of the transition in the system of a free sphere freely moving in a fluid under the action of gravity. This physics is captured in an optimal way using a spectral azimuthal decomposition. It is this particular method of discretization that makes the resulting code limited in the variety of application on one hand and extremely efficient on the other hand. If other applications are aimed at, the underlying NS solver has to be adapted. Whenever possible, it is obviously preferable to avoid moving meshes. For non-spherical but axisymmetric bodies, a rotating system is the way out – see e.g. [8]. In this way, the interesting problem of a free falling solid ellipsoid could be tackled similarly as in [8] for a non-deformable bubble. The price paid is the necessity to use a full spherical computational domain. If, moreover, the advantage of the axisymmetric geometry is lost the cost increase may be higher, but not more than 100% (if the solution of the Stokes-like problem (56) can no longer benefit from the azimuthal decomposition). To deal with two or more particles, moving meshes cannot be avoided. In that case, a solver of the type ALE or DLM cited in the introduction is probably a very good choice. Even these solvers will, however, either fail if light particle equations of motion are not dealt with implicitly, or, be unnecessarily costly if the implicit formulation is enforced iteratively. We explained the reasons and proposed a way out of this difficulty.

Acknowledgements

The authors are grateful for the possibility to run a part of the numerical tests presented in this paper on the MetaCenter supercomputing facilities provided under the research grant MSM 0000000001 of the Czech Republic.

References

[1] B. Ghidersa, J. Dušek, Breaking of axisymmetry and onset of unsteadiness in the wake of a sphere, J. Fluid Mech. 423 (2000) 33–69.
[2] A. Tomboulides, S. Orszag, G. Karniadakis, Direct and large-eddy simulation of axisymmetric wakes, AIAA – 31st Aerospace Sciences Meeting & Exhibit, 1993, pp. 1–12.
[3] D. Karamanev, C. Chavarie, R. Mayer, Dynamics of the free rise of a light solid sphere in liquid, AIChE J. 42 (6) (1996) 1789–1792.
[4] M. Jenny, G. Bouchet, J. Dušek, Non vertical ascension or fall of a free sphere in a newtonian fluid, Phys. Fluids 15 (1) (2003) L9–L12.
[5] H.H. Hu, Direct simulation of flows of solid–liquid mixtures, Int. J. Multiphase Flow 22 (2) (1996) 335–352.
[6] N. Patankar, T. Ko, H. Choi, D. Joseph, A correlation for the lift-off of many particles in plane Poiseuille flows of newtonian fluids, J. Fluid Mech. 445 (2001) 55–76.
[7] R. Glowinski, T. Pan, T. Hesla, D. Joseph, J. Périaux, A fictitious domain approach to the direct numerical simulation of incompressible viscous flow past moving rigid bodies: application to particulate flow, J. Comput. Phys. 169 (2001) 363–426.
[8] G. Mougin, J. Magnaudet, Path instability of a rising bubble, Phys. Rev. Lett. 88 (2002) 014502.
[9] S.A. Orszag, A.T. Patera, Secondary instability of wall-bounded shear flows, J. Fluid Mech. 128 (1983) 347–385.
[10] J. Lopez, F. Marques, J. Shen, An efficient spectral-projection method for the Navier–Stokes equations in cylindrical geometries, J. Comput. Phys. 176 (2) (2002) 384–401.
[11] M. Jenny, G. Bouchet, J. Dušek, Influence of instabilities on the trajectory of a light sphere, ASME FED Summer Meeting, Montréal, Canada.

[12] R. Natarajan, A. Acrivos, The instability of the steady flow past spheres and disks, J. Fluid Mech. 254 (1993) 323–344.
[13] M. Wu, M. Gharib, Experimental studies on the shape and path of small air bubbles rising in clean water, Phys. Fluids 14 (7) (2002) L49–L52.
[14] K. Lunde, R.J. Perkins, Observations on wakes behind spheroidal bubbles and particules, ASME Fluids Engineering Division Summer Meeting FEDSM'97 (FEDSM97-3530).